

**PROCESS CHARACTERIZATION OF HYDROGEN DIRECT  
REDUCTION OF STAINLESS STEEL OXIDES**

A Thesis  
Presented to  
The Academic Faculty

by

Cole Hardy Burton

In Partial Fulfillment  
of the Requirements for the Degree  
Master of Science in the  
School of Materials Science and Engineering

Georgia Institute of Technology  
December 2025

**COPYRIGHT © 2025 BY COLE BURTON**

**PROCESS CHARACTERIZATION OF HYDROGEN DIRECT  
REDUCTION OF STAINLESS STEEL OXIDES**

Approved by:

Dr. Robert Speyer, Advisor  
School of Materials Science and  
Engineering  
*Georgia Institute of Technology*

Dr. Joshua Kacher  
School of Materials Science and  
Engineering  
*Georgia Institute of Technology*

Dr. Naresh Thadhani  
School of Materials Science and  
Engineering  
*Georgia Institute of Technology*

Date Approved: November 29, 2025

## ACKNOWLEDGEMENTS

First and foremost, I would like to thank my family for their love and caring. I would not be in the position I am in today without their continued support and dedication to my wellbeing. When my health and body have failed me, my family has not. I have always been able to rely on them when I needed them most and have enabled me to overcome so many obstacles that I would not have been able to surmount alone. I would also like to thank my advisor, Dr. Robert Speyer, for granting me so many opportunities and for instilling a deep appreciation for and fascination with thermodynamics and our discipline in total. I began my time with Dr. Speyer first as teaching assistant and later became his research assistant. My respect for and trust in Dr. Speyer as a researcher and professor grows daily. His breadth and depth of knowledge inspire me to be as wise, intelligent, and patient as I know him to be. His personal significance as my advisor in my life cannot be understated. I would also like to thank the rest of my committee, Dr. Joshua Kacher and Dr. Naresh Thadhani, for providing helpful feedback and resources throughout the duration of my time on the project. I have to thank Samrin Saiyara for holding our furnace consultations in the campus pottery studio. I would have run out of gas tanks, extrusions, and sanity without the help and friendship of Alec Balandin. I would also like to thank Neyton Baltodano, Apurva Nayak, and William Carlton for their assistance in extrusions and other contributions. Yolande Berta and David Tavakoli have aided me many times in the characterization of my samples. I would also like to thank our sponsors at ARPA-E, Toni Marechaux and Cory Phillips, for our constructive meetings on the project.

# TABLE OF CONTENTS

<b>ACKNOWLEDGEMENTS</b>	<b>1</b>
<b>LIST OF TABLES</b>	<b>3</b>
<b>LIST OF FIGURES</b>	<b>4</b>
<b>CHAPTER 1. Introduction</b>	<b>7</b>
<b>CHAPTER 2. Background</b>	<b>9</b>
2.1.1 Metal-Oxide Equilibrium	10
2.1.2 Organic Components	14
2.1.3 Ore Utilization	15
2.1.4 Hydrogen Safety	16
<b>CHAPTER 3. Experimental Procedure</b>	<b>18</b>
3.1.1 Raw Materials and Green Body Processing	18
3.1.2 Thermogravimetric Analysis	19
3.1.3 Reduction and Sintering Heat Treatments	20
3.1.4 Characterization	22
<b>CHAPTER 4. Results</b>	<b>23</b>
4.1.1 Thermogravimetric Analysis	23
4.1.2 Thermolysis and Sintering Heat Treatments	33
4.1.3 X-Ray Diffraction	34
4.1.4 Scanning Electron Microscopy & Energy-Dispersive Spectroscopy	39
<b>CHAPTER 5. Discussion</b>	<b>41</b>
<b>CHAPTER 6. Conclusions and Future Work</b>	<b>44</b>
<b>REFERENCES</b>	<b>47</b>

## LIST OF TABLES

Table 1	Comparison of metal and metal oxide species density.	11
---------	--	----

## LIST OF FIGURES

Figure 1	A unit cell of the spinel crystal structure. Red corresponds to $O^{2-}$ , orange $Fe^{2+}$ , and grey $Cr^{3+}$ .	12
Figure 2	Raoultian solutions of Fe-Cr in equilibrium with FeO-Cr <sub>2</sub> O <sub>3</sub> at various temperatures. Courtesy of R. Speyer	13
Figure 3	The chemical structure of methyl cellulose	14
Figure 4	A typical extrusion product, laid flat to dry. (credit: A. Balandin)	19
Figure 5	Temperature-controlled thermogravimetric analysis of extrudate fragments in static air, with a heating rate of 2 °C/min and high temperature hold at 400 °C for 60 minutes. This mass curve indicates a mass loss of 9.8 wt.%.	23
Figure 6	Mass-loss-rate-controlled thermogravimetric analysis of extrudate fragments in static air, with a setpoint mass loss rate of 1.5 wt.%/hr. This mass curve indicates a mass loss of 8.9 wt.% over 6 h.	24
Figure 7	Mass-loss-rate-controlled thermogravimetric analysis of extrudate fragments in static air, with setpoint a mass loss rate of 0.75 wt.%/hr. This mass curve indicates a mass loss of 8.8 wt.% over 12 h.	25
	Linear cellular alloy oxide green body produced by Nadler et al	26
Figure 8		
Figure 9	Temperature-controlled thermogravimetric analysis of legacy project sample fragments in static air, with a heating rate of 2 °C/min and high temperature hold at 400 °C for 60 minutes. This mass curve indicates a mass loss of 4.78 wt.%.	27
Figure 10	Mass-loss-rate-controlled thermogravimetric analysis of extrudate fragments in static air, with a setpoint mass loss rate of 0.3 wt.%/hr. This mass curve indicates a mass loss of 3.8 wt.% over 6 h.	28
Figure 11	Mass-loss-rate-controlled thermogravimetric analysis of extrudate fragments in static air, with a setpoint mass loss rate of 0.3 wt.%/hr. This mass curve indicates a mass loss of 3.8 wt.% over 11 h.	29
Figure 12	Temperature-controlled thermogravimetric analysis of printed part fragments in static air, with a heating rate of 2 °C/min and high	30

temperature hold at 400 °C for 60 minutes. This mass curve indicates a mass loss of 28.9 wt.%

- Figure 13 Mass-loss-rate-controlled thermogravimetric analysis of printed part fragments in static air, with a setpoint mass loss rate of 4.42 wt.%/hr. This mass curve indicates a mass loss of 26.6 wt.% over 6 h. Thermolysis occurs mainly at two temperatures, 172 °C and 330 °C. 31
- Figure 14 Mass-loss-rate-controlled thermogravimetric analysis of printed part fragments in static air, with a setpoint mass loss rate of 2.25 wt.%/h. This mass curve indicates a mass loss of 27 wt.% over 12 h. Thermolysis occurs mainly at two temperatures, 156 °C and 300 °C. 32
- Figure 15 Temperature-controlled thermogravimetric analysis of high solids formulation sample fragments in static air, with a heating rate of 2 °C/min and high temperature hold at 400 °C for 60 minutes. This mass curve indicates a mass loss of 3.21 wt.%. 33
- Figure 16 Powder X-ray diffraction curves for different tested furnace routes. Identified peaks are labeled as h = hematite; e = eskolaite; c = chromite; f =  $\alpha$ -iron; i = synthetic iron; g =  $\gamma$ -iron. Effectively all hematite has been reduced by 950 °C. 35
- Figure 17 Powder X-ray diffraction curves for different tested furnace routes. Identified peaks are labeled as h = hematite; e = eskolaite; c = chromite; f =  $\alpha$ -iron; i = synthetic iron \* = unidentified 36
- Figure 18 Powder and Bulk X-ray diffraction curves for different tested furnace routes. Powder bed XRD was performed on the 1150 °C sample, and bulk XRD was chosen for the 1200 and 1250 °C samples. Identified peaks are labeled as h = hematite; e = eskolaite; c = chromite; f =  $\alpha$ -iron; i = synthetic iron; g =  $\gamma$ -iron, s = silicon 37
- Figure 19 Bulk X-ray Diffraction curves for tested different furnace routes. Identified peaks are labeled as h = hematite; e = eskolaite; c = chromite; f =  $\alpha$ -iron; i = synthetic iron; g =  $\gamma$ -iron, s = silicon 38
- Figure 20 Bulk X-ray Diffraction curves for tested different furnace routes. Identified peaks are labeled as h = hematite; e = eskolaite; c = chromite; f =  $\alpha$ -iron; i = synthetic iron; g =  $\gamma$ -iron. 39
- Figure 21 EDS spectra with calculated weight percent of elements identified for a ground and polished specimen heat-treated at 1250 °C for 4 h. 40
- Figure 22 Reduced low solids sample mounted in conductive epoxy for use in an SEM 40

## SUMMARY

Fabrication of complex stainless-steel components using conventional melting and forming methods is often limited by geometric constraints, high energy consumption, and tooling costs. This study investigates the direct hydrogen reduction and sintering of metal–metal oxide extrusions designed to replicate the composition of 316L stainless steel. Extruded samples containing varying solids loadings and organic binders were characterized using X-ray diffraction (XRD), energy-dispersive spectroscopy (EDS), and thermogravimetric analysis (TG) to monitor thermolysis, reduction and sintering. Full reduction of iron and nickel oxides was achieved at or before 950 °C, while chromium oxide formed spinel phases, reduced to chromium metal as a member of the iron solid solution, or remained as eskolaite (a polymorph of  $\text{Cr}_2\text{O}_3$ ). The sintering temperature and time required for densification were correlated with extrudate composition; higher solids loading require a higher hold of 1250 °C, whereas lower solids content allows for a lower 1200 °C process temperature. Higher temperatures and longer dwell times resulted in a higher proportion of austenite compared to ferrite. This process enables fabrication of complex thin-walled geometries with reduced energy consumption and lower tooling requirements compared to traditional stainless steel manufacturing techniques. These results provide a foundation for extending hydrogen-based reduction to other alloy systems, including nickel-based superalloys, and highlight the potential for increased domestic, water-based emission metal production.

## CHAPTER 1. INTRODUCTION

Complex cross sectional geometries of structural parts offer impressive specific strength and stiffness, improving upon the performance of both regular hollow tubes and standard I-beams. This is due to their unique internal structures that provide support and load sharing across the part.

Extrusion of steel billets is intensive, as it often requires elevated temperatures for hot extrusion and extreme pressures, up to 1300 °C and 700 MPa for some steels [4]. This also requires the metal to be reduced from their ores and formed into billets beforehand. In powder metallurgy, these powders can often pose health risks in the form of heavy metals, like Cd, Ni, Pb, etc., or fire and general reactivity risk as metals like Ti, Al, Si. By forming extrusions from oxides and reducing them in-situ with a sintering heat-treatment, the energy, processing, and exposure risk can be minimized.

This work focuses on a blend of metal and metal oxide powders, intended to match the final composition of austenitic stainless-steel grade 316L. This alloy was selected due to its utilization in structural, medical, and marine applications. Iron, nickel, and chromium powders are provided in their oxide form ( $\text{Fe}_2\text{O}_3$ ,  $\text{NiO}$ ,  $\text{Cr}_2\text{O}_3$ ) and molybdenum and manganese are added as metal powders. Organics are used to bind and lubricate the extrusion and are combusted away in air before reduction. Previous work by Nadler et al. indicates that the reduction and solid-solution incorporation of chromium (16-18%) into

the metallic matrix is achievable due to the presence of the iron metal, as it catalyzes the reduction of chromia and allows for lower  $p_{\text{H}_2\text{O}}$  to  $p_{\text{H}_2}$  ratio of reduction.

This work has focused on the removal of the binder, and the reduction & sintering of the strips of metal oxide extrusions, to find and characterize a furnace route that minimizes, time, temperature, and hydrogen gas concentration. TG was selected to determine the thermal decomposition behavior of the organic components of the extrusions, and XRD peak attribution and SEM and EDS maps were chosen to confirm the presence of gamma iron and alloying elements

The elemental components being present as discrete particles presents challenges with complete reduction and sintering being competing processes as the extrudate is furnaceed. Some porosity at the beginning may be desirable to allow for easy gas exchange between the water exhaust and reducing hydrogen. In this scenario, the metals interdiffuse in the solid state only, so uniformity in elemental distribution is determined by initial particle size and distribution and the extent that the species may diffuse.

After achieving reduction of metal oxide samples, multi-step holds were used to investigate the phase progression of metal oxide mixture into metal alloy. The results of these experiments are presented later.

## CHAPTER 2. BACKGROUND

Extrusion of metal oxide paste is particularly attractive due to the drastic reduction in pressures and machining of dies required, compared to hot extrusion of a reduced alloy of a similar composition. The ability to remain below the melting temperature of the alloy while reducing the ore drastically reduces the stress of the process normally used to produce steel or other metal alloys.

This alloy composition was chosen to replicate the one found in traditionally manufactured 316L, which typically involves the selective oxidation of the dissolved carbon to achieve a lower carbon content than created by blast furnaces. Carbon content removed this way is generally carried out in a basic oxygen furnace, that uses precise  $p_{O_2}$  control to oxidize select impurities in molten steel into a slag and gas that can be removed [4].

Historically, direct reduction studies tended to focus on binary mixtures in order to prove that the presence of other metals would in fact catalyze the reduction of less noble metals like chromium in the presence of iron. Thus, after chromium alloys being successfully produced in studies like Nadler et al. [17], an alloy composition of austenitic stainless steel 316L was chosen as a desirable and chemically possible to produce alloy. This composition contains less than 33% by weight of alloying elements, which includes the low carbon content, below 0.03%. This incredibly low carbon ceiling is implemented to improve welds and their longevity, which would be a likely manufacturing technique for affixing the proposed honeycomb structures. The lack of carbon present in the metal prevents chromium from segregating into carbides at grain boundaries, which would

negatively impact the steel's intergranular corrosion resistance after a high-temperature process like welding [4].

### *2.1.1 Metal-Oxide Equilibrium*

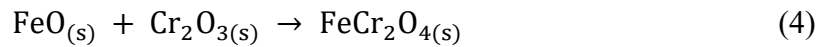
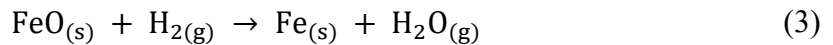
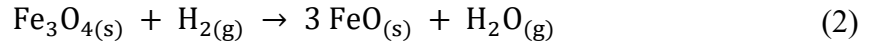
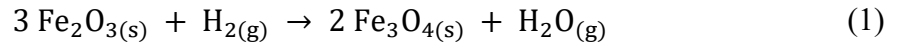
Chromium-containing alloys pose a challenge to the complete reduction of the entire oxide body. Hydrogen reduction of oxides such as chromia is thermodynamically possible, but more difficult compared to the readily reduced iron and nickel present in the alloy system, due to temperatures required and kinetics of reaction. Other specialized steels contain other metals that are hard to reduce with hydrogen at elevated temperatures, such as the titanium or aluminum normally contained in the nickel precipitates that give maraging steel its exceptional yield strength. [5]

Iron bearing minerals typically incorporate it in its +2 or +3 oxidation state. Throughout the reduction of hematite to iron metal, it must pass sequentially through its oxidation states, listed in Equations 1-4. This also includes the 1:1 stoichiometric mixture of hematite and wüstite, magnetite ( $\text{Fe}_3\text{O}_4$ ). Pure hematite begins to densify after transforming to magnetite, after which it will reduce to wüstite and then eventually iron metal, transforming into austenitic, gamma iron upon heating to approximately 910 °C, which is retained at low temperatures due to the presence of Ni and Mn [5,12,15]. The evolution of the molar volume presented in Table 1 demonstrates the densification induced by the reducing conditions in the structure, and the contraction experienced by the metal oxide over time. The structure depicted in Figure 1 is representative of the more complex nature of spinel structures, compared to the pure oxide of each component. Iron oxides also

adopt a related structure of inverse spinel, in which corresponding cations in AB<sub>2</sub>O<sub>4</sub> composition replace for an effective structure of B(AB)O<sub>4</sub>.

**Table 1: Comparison of metal and metal oxide species density. [5,12,20]**

	(Eskolaite) ) Cr <sub>2</sub> O <sub>3</sub>	(Hematite) ) Fe <sub>2</sub> O <sub>3</sub>	(Magnetite) ) Fe <sub>3</sub> O <sub>4</sub>	(Wüstite) ) FeO	(Chromite) ) FeCr <sub>2</sub> O <sub>4</sub>	(Ferrite) ) α-Fe	(Austenite) ) γ-Fe
Crystal Structure	Hexagonal	Hexagonal	Cubic (inverse spinel)	Cubic (rocksalt)	Cubic (spinel)	Cubic (BCC)	Cubic (FCC)
Density (g/cm <sup>3</sup> )	5.22	5.26	5.197	6.017	5.056	7.874	7.647
Molar Mass (g/mol)	151.99	159.69	231.54	71.85	223.833	55.845	55.845
Molar Volume (cm <sup>3</sup> /mol)	29.117	30.359	44.553	11.9	44.27	7.092	7.303



Chromium oxide, also known as chromia or the mineral eskolaite, begins in its +3 oxidation state as well. Not having a stable oxidation states less than +3, it must transition either directly to metal when exposed to reducing conditions or enter a complex oxide with other species. The mechanism by which chromium is effectively reduced is related to both Le Chatelier's Principle & a decrease in Gibbs free energy due to the entropy of mixing. Chromium oxide at furnace temperature will not reduce appreciably alone, but the presence

of iron metal allows for the depletion of the small amounts of chromium metal produced by reduction, introducing it into the metal solid solution. This, and the doping of  $\text{Cr}^{3+}$  into wüstite before reduction are responsible for the reduction that occurs in the alloy [17]. Additionally, when metals are in contact with electrical insulators or semiconductors, band bending of the electronic structure of the nonmetal occurs in response to the electrical contact with the metal. Localized changes in Fermi level and the valence band facilitate the reduction of the less noble chromium oxide, reducing the energy barrier for electron excitation [23].

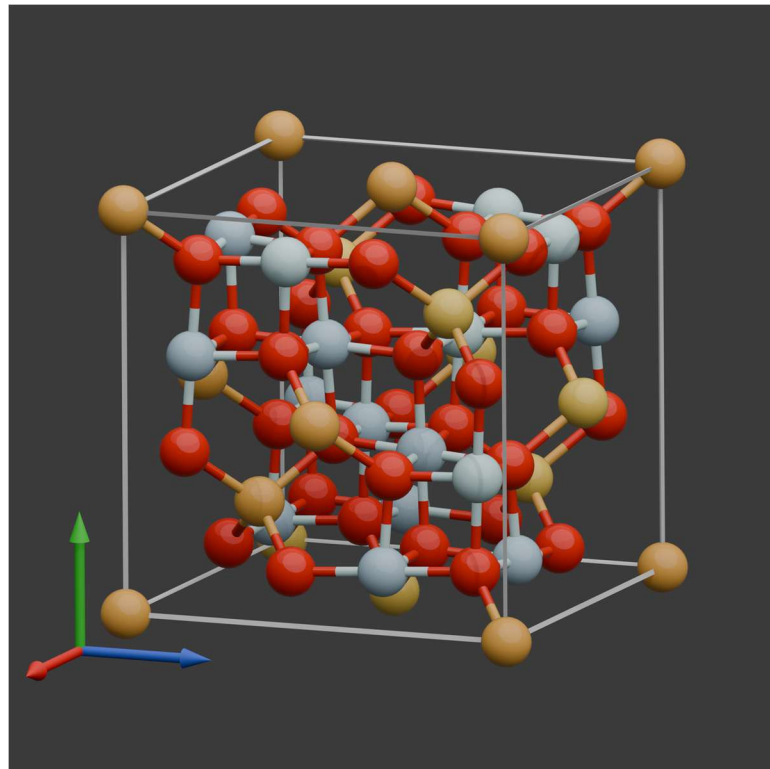


**Figure 1:**A unit cell of the spinel crystal structure. Red corresponds to  $\text{O}^{2-}$ , orange  $\text{Fe}^{2+}$ , and grey  $\text{Cr}^{3+}$ .

Considering the two primary elements in 316L, iron and chromium, ideal solutions of both the oxides and metal can be considered. When in equilibrium at the elevated temperatures

of reduction, the alloy can contain upwards of 18% by mole fraction Cr metal, in an appropriately reducing environment. This calculation is displayed in Figure 2.

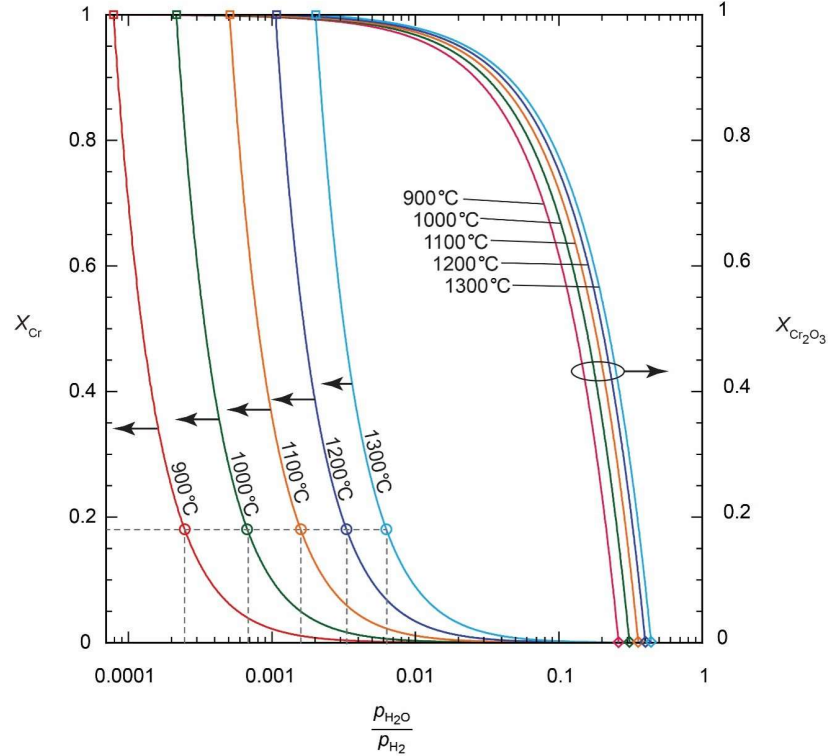


**Figure 2: Raoultian solutions of Fe-Cr in equilibrium with FeO-Cr<sub>2</sub>O<sub>3</sub> at various temperatures. Courtesy of R. Speyer [6]**

Both iron and chromium are naturally found in the mineral named chromite, a spinel in the form of FeCr<sub>2</sub>O<sub>4</sub>. This oxide is also a product of the co-reduction of chromium and iron oxides. It is a more stable oxide than eskolaite, so a higher temperature or higher p<sub>H2</sub>/p<sub>H2O</sub> would be required to reduce this species [13]. The reaction between dissolved chromium and chromite results in the reduction of the Fe<sup>2+</sup> cation present in the chromite to iron metal, and the oxidation of dissolved chromium back to chromium oxide. Nickel oxide, present in its form of bunsenite, starts off in its +2 oxidation state before reduction. The presence of these other metals and metal oxides may affect the final structure of the metal matrix,

but also which oxides are preferentially produced when coreducing the entire alloy together.

### 2.1.2 Organic Components

Methyl cellulose, or its IFF owned-brand name Methocel, is a long chain polymer that is water soluble and used as a binder in the oxide mixture. It is chemically modified cellulose, with some of the hydroxyl groups of typical glucose ring being replaced by methoxide, (-OCH<sub>3</sub>) groups. Ether bonds depicted in Figure 3 (-COC-) are a strong covalent bond and therefore do not start breaking down until above 300 °C. Depending on the degree of substitution of the methoxide groups, the dehydration reaction of the hydroxyl groups will also take place at temperatures above 150 °C [16].

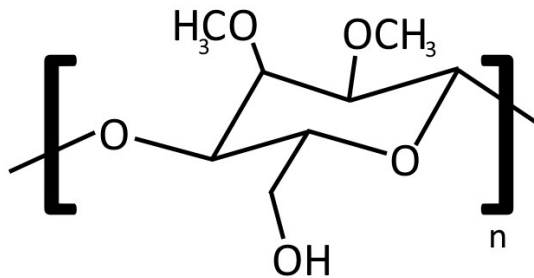


**Figure 3: The chemical structure of methyl cellulose**

The other organics, used in significantly lower quantities, are other polymeric agents. DARVAN-C, used in trace amounts is a polymer salt of polymethacrylate. This is a simpler polymer than Methocel, with no rings but ester side groups. PLGA, or poly(lactic-co-glycolic) acid is a water-soluble block copolymer of glycolic and lactic acid. Pegosperse-100S is a water-soluble emulsifier, used in this case as a lubricant for the extrudate. This is diethylene glycol stearate, a water-soluble stearic acid group joined to a

short, polyethylene group. All the organics present contain at least one kind of strong carbon-oxygen covalent bond that will delay or extend the temperature range of mass evolution, compared to simple hydrocarbons. However, unsaturated bonds will still release several times their solid volume in volatiles at lower temperatures, which can introduce cracks or holes into the part that are not healed during reduction and sintering. If performed rapidly in the presence of oxygen, the exothermic nature of combustion can result in the explosive removal of organics and introduce cracks.

Carbon-containing species either volatilize, oxidize, or remain as carbon char. To succeed in making 316L, the final carbon content of the metal must remain below 0.03% [12]. Considering the initial organics loading of extrudate, this may not be achievable solely through volatilization and inert thermolysis. Char is of most concern due to its remnants being in close contact with metal oxide particles in the solid state. It is possible that if char were to remain between chromium and iron oxide, it may preferentially form carbides that sequester the chromium and prevent it from entering the solid solution. This could lead to sensitization at boundaries between former oxide particles, likely leading to intergranular corrosion later.

### *2.1.3 Ore Utilization*

Metallic elements most often appear in Earth's crust in a range of mixed oxide compounds, ranging from pure oxides like hematite and magnetite, to spinels and silicates. Beneficiation and refinement of such minerals can prove to be a cumbersome task, involving numerous mechanical, physical and chemical separation techniques to reach desired purity. Eisele has investigated the usage of both aerobic and anaerobic bacterial

environments to refine iron ore through iron reduction and phosphorus depletion [8]. Iron oxide can be successfully extracted from more extensive sources, including many domestic sources that are currently too phosphorus-rich to be considered useful, decreasing its potential for poor weldability and embrittlement that come with high inherent phosphorus content. Additionally, lower iron concentration tailings from traditional manufacturing waste streams could be considered as a potential source of iron minerals to create steel with.

#### *2.1.4 Hydrogen Safety*

Hydrogen gas, while used in many industries safely, can pose a significant safety hazard, especially in a high temperature environment like industrial steel production. In addition to safety concerns, improper processing of steel in hydrogen environments can lead to hydrogen embrittlement of parts. Hydrogen fires are nearly invisible, emitting light in the near ultraviolet range, and can sustain ignition at volume concentrations from 4% to 75%. This range is significantly wider than most traditional fuels and is complicated further by the ease of hydrogen ignition [1]. Due to hydrogen's sensitivity to oxygen present in the atmosphere, balancing the presence of inert gas and hydrogen is important to the safety and efficiency of an industrial process. Inert gases must be extracted from the atmosphere, collected and processed with Joule-Thompson throttling, and separated through cryogenic fractional distillation to ensure high purity. While hydrogen's abundance is a non-issue, as it can be made electrolytically from water, clean and efficient sources of hydrogen are of concern, as some production methods require separate power, handling, and sometimes emissions in the case of steam-methane reforming (SMR) [22].

When a hypothetical stainless steel alloy and its oxide is in equilibrium with hydrogen gas and water vapor, the ratio between hydrogen and water is in the order of several degrees of magnitude ( $10^{-3}$ ). This represents an extremely inefficient conversion rate in terms of moles of gas expelled for reduction of FeO or Cr<sub>2</sub>O<sub>3</sub>. On an industrial scale, it could prove useful to recycle the flue gas. By condensing the water out of exhaust gas, the optimal ratio of inert and hydrogen could be maintained and cycled back through the furnace system with supplemental hydrogen added back in as balance. Continuous analysis of the exit gas could also be helpful in determining the rate of reduction as well as when the reduction has effectively stopped.

## CHAPTER 3. EXPERIMENTAL PROCEDURE

### *3.1.1 Raw Materials and Green Body Processing*

Ribbon samples of extruded green bodies were provided by the Kacher Group (MSE, Georgia Tech). Powders used by weight percentage were 63.37% Fe<sub>2</sub>O<sub>3</sub> (hematite, 96%, Sigma-Aldrich, <5 μm), 8.236% NiO (bunsenite), and 17.03% Cr<sub>2</sub>O<sub>3</sub> (eskolaite, 98%, Sigma-Aldrich <50 μm,) were mixed with metal powders of 1.294% Mo (molybdenum metal, 99.95%, ThermoScientific, 3-7 μm) and 0.9766% Mn (manganese metal, 99.6%, Alfa-Aesar, <10 μm). These were put in aqueous suspension of deionized water, along with 9.1% organic binder Methocel (methyl-cellulose). The solids loading was calculated to be 34.01% by volume.

In subsequent recipes for optimization of extrusion, batches were created with a higher solids loading, 55% by volume. Methocel content was decreased to 2.5% by weight and 0.43% of the water-soluble lubricant, Pegosperse-100S (VWR) was dissolved into the deionized water. The paste was homogenized through paddle mixing and extruded through a slot die to produce rectangular prisms of ribbons of extrudate. The ribbons were left to air dry. A drying sample is displayed in Figure 4.



**Figure 4: A typical extrusion product, laid flat to dry. (credit: A. Balandin)**

### *3.1.2 Thermogravimetric Analysis*

Initial heat-treatment of the green body extrudates acted to remove the organics used to facilitate extrusion and give the green body handling strength. If these organics are volatilized too quickly, the part can distort or crack. Thermogravimetric analysis (TG, measurement of in-situ weight change during heat-treatment) is useful for determining the temperature ranges over which these organics are rapidly extracted. These were performed in air, so that the extraction was a combustion process.

Approximately 50 mg sections the extruded bodies were characterized using thermogravimetric analysis. Samples were heated at 2°C/min raised to 400°C and held for one hour. In addition, the software in the TG system permitted rate-controlled thermogravimetry. Proportional-integral-derivative (PID) feedback control was applied to the weight loss. In this way, heating element power was adjusted so that specimen weight loss followed a setpoint rate. The resulting temperature profile shows slow heating in temperature ranges in which organic extraction was rapid, and relatively faster heating in

which organic extraction attenuated. This temperature profile can then be programmed into the thermolysis step of a furnace so that organic extraction from a part is undertaken with precision and efficiency while minimizing conditions that would result in part warpage, or cracking.

### *3.1.3 Reduction and Sintering Heat Treatments*

A MoSi<sub>2</sub> heating element furnace was used for heat treatments. Specimens were placed on Al<sub>2</sub>O<sub>3</sub> setters in a closed ended tube Al<sub>2</sub>O<sub>3</sub> tube of 10 cm diameter. An aluminum collar was placed on the open end of the tube which extended out of the furnace. That collar made a gas-tight seal via rubber O-rings, water cooled by refrigerated water flowing between parallel O-rings. The collar had another gas-tight seal to a closed-ended alumina tube in which an S-type thermocouple was fed into, with the thermocouple junction located within the hot zone along the length of the furnace tube. Gas-tight gas feedthroughs were also part of the end cap. These were either entry and exit ports for compressed air used during thermolysis heat-treatments, or helium/hydrogen mixtures used during reduction and sintering heat-treatments.

Programmable digital mass flow controllers (Alicat MC-2SLPM-D) were placed on separate compressed H<sub>2</sub> and He gas cylinders. The gas flows from these were combined in a T-connection to a single line which fed into the furnace. Stainless-steel Swagelok quick-connects were affixed to allow for easier handling of the collar and thermocouple. The mixture entering the furnace flowed through an interior alumina tube so that it emerged at the hot zone of the furnace within the furnace tube. The exit gas had no such extender tube. That gas ran through a copper tube for 38 cm and then transitioned to plastic tubing

in a path that led to a fume hood. The copper tubing was for the purpose of initial cooling of the exiting furnace gas. Within the fume hood was a digital gas flow monitor that the gas ran through before entering a flask with a glass tube leading to water that the gas bubbled through. This was used to prevent back-flow of atmospheric oxygen into the furnace. The exiting gas was evacuated to the building exterior through a fume hood.

RS485 serial communications from the two mass flow controllers and the mass flow monitor were fed into a computer and were utilized by the same software that operated the furnace. To facilitate the safe use of hydrogen, protection features were incorporated into the software. The furnace heat-treatment setpoint scheduling required specification of whether He and/or H<sub>2</sub> were used for a given step in the schedule. A schedule using H<sub>2</sub> was not permitted unless it was preceded and followed up with a pure, He schedule. The preceding schedule was to purge O<sub>2</sub> out of the furnace chamber, and the following schedule was to purge H<sub>2</sub> out of the furnace before the furnace could be opened to the atmosphere. The furnace run was triggered to terminate if the flow in the fume hood was monitored to fall below 75% of the sum of setpoint He and H<sub>2</sub> mass flow rates, implying a gas leak in the furnace tube.

For the first step of thermolysis, a ramp rate of 5.4 °C/min was used to 285 °C with a 145-minute hold at was determined from TG data. Slower ramps of 0.25 and 0.5 °C/min were maintained for 125 minutes and 65 minutes, respectively, to a final temperature of 345 °C. A ramp rate of 5°C/min was used to initiate all runs, using He only at a flow rate of 1 SLPM. Starting at 400°C, H<sub>2</sub> was introduced. After holding for specified times, cooling ramp rates of 5 °C/min were used to 800 °C and of 3 °C/min were used to 300 °C under low flowing He to prevent the cooling furnace chamber gas from forming a negative

pressure condition that would draw bubbler liquid and/or air into the furnace. A series of dwell temperatures and times, as well as H<sub>2</sub>/He ratios were investigated. 2 standard liters per minute of helium were used during reduction steps, and concentrations of 5%, 10%, and 20% H<sub>2</sub> were tested before utilizing 20% for most samples.

#### *3.1.4 Characterization*

Specimens removed from the furnace after heat-treatments were analyzed using X-ray diffraction (XRD). Specimens whose heat-treatment did not result in extensive sintering were crushed into a powder in an alumina mortar and pestle and then placed in the depression of a zero-background, {111} angled silicon crystal powder holder, and gently pressed flat with a glass slide. Specimens were analyzed (Rigaku Miniflex Powder XRD), scanning from 10-100° 2θ at a rate of 1° per minute. All scans were collected in X-ray fluorescence reduction mode, to account for the Cu K-alpha x-ray beam causing strong fluorescence in the present metals and oxides.

Specimens which demonstrated extensive sintering were mounted as a single piece hot-mounting in epoxy in and the surface of the specimen was ground away, or hand ground and polished. Those specimens were then mounted in the x-ray diffractometer for analysis.

Selected specimens were mounted in conductive epoxy and placed into an SEM with copper tape in minimal contact with the edge of the sample. An analysis of the elemental constituents present was performed using energy-dispersive spectroscopy.

## CHAPTER 4. RESULTS

### 4.1.1 Thermogravimetric Analysis

After drying, shards of extrudate were heat-treated in the thermogravimetric analyzer (TG) in static air, as shown in Figure 5. The sample lost ~10% of its weight, mostly between 267 and 400 °C.

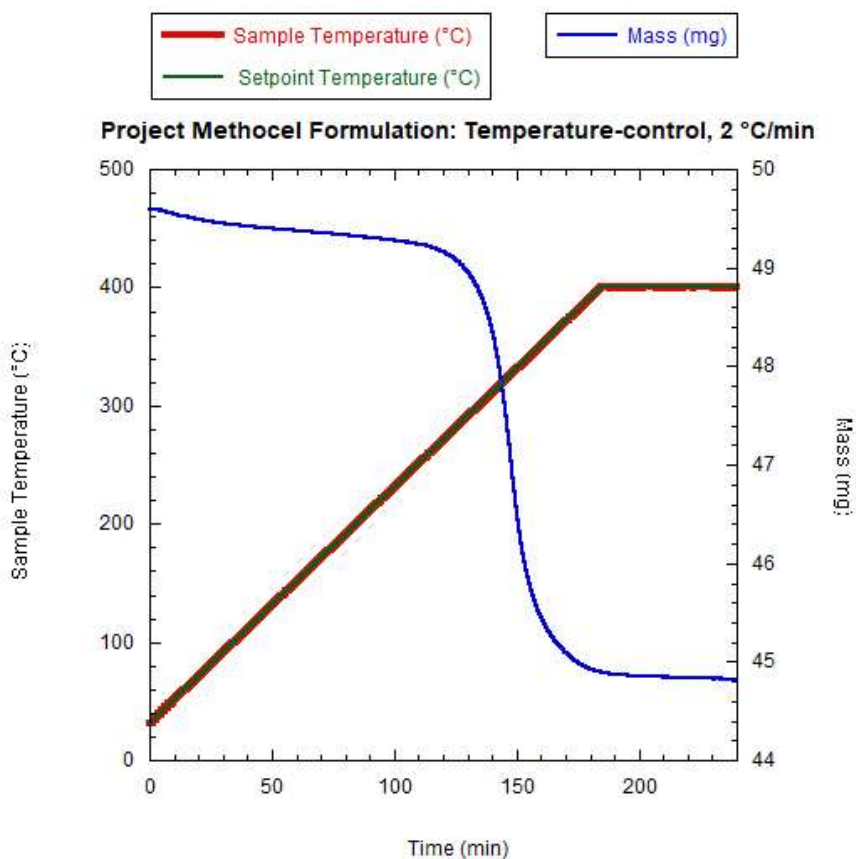


**Figure 5: Temperature-controlled thermogravimetric analysis of extrudate fragments in static air, with a heating rate of 2 °C/min and high temperature hold at 400 °C for 60 minutes. This mass curve indicates a mass loss of 9.8 wt.%.**

Based on this total weight loss identified from temperature-controlled TG, subsequent experiments were performed using rate-controlled TG. Two different set-point weight loss rates of 1.5 wt.%/h and 0.75 wt.%/h were undertaken, as shown in Figures 6 and 7, respectively. The second was designed to facilitate a more gradual extraction of the organics. For both, temperature rose rapidly to approximately 290 °C. At this temperature range, organic extraction was relatively rapid, hence furnace power was adjusted so that extraction was, for a period, isothermal, and then followed by a gradually accelerating increase in temperature.

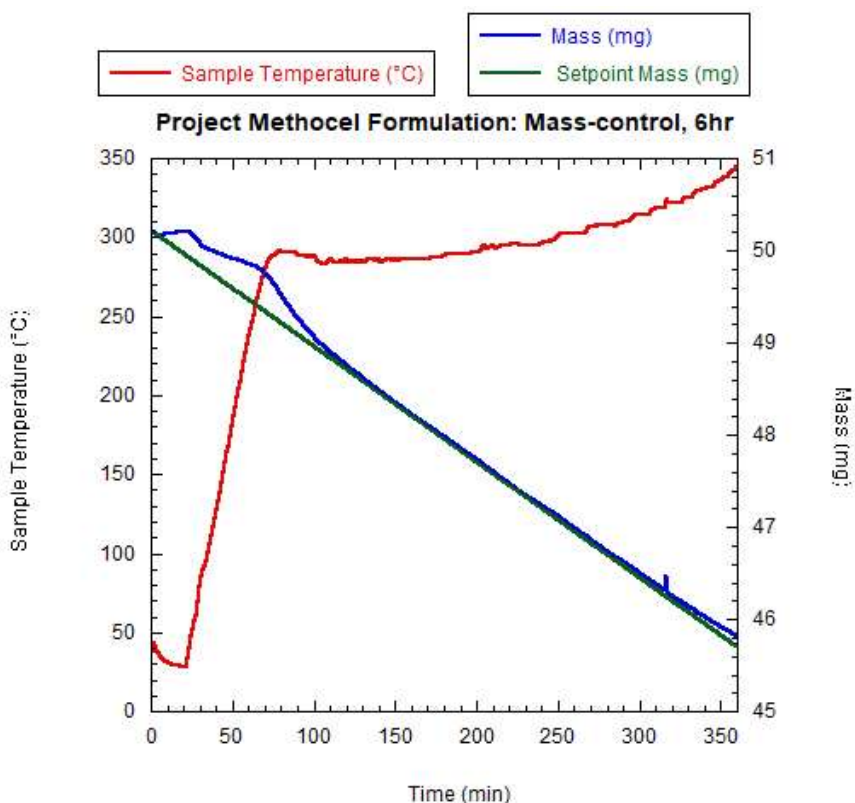


**Figure 6: Mass-loss-rate-controlled thermogravimetric analysis of extrudate fragments in static air, with a setpoint mass loss rate of 1.5 wt.%/hr. This mass curve indicates a mass loss of 8.9 wt.% over 6 h.**

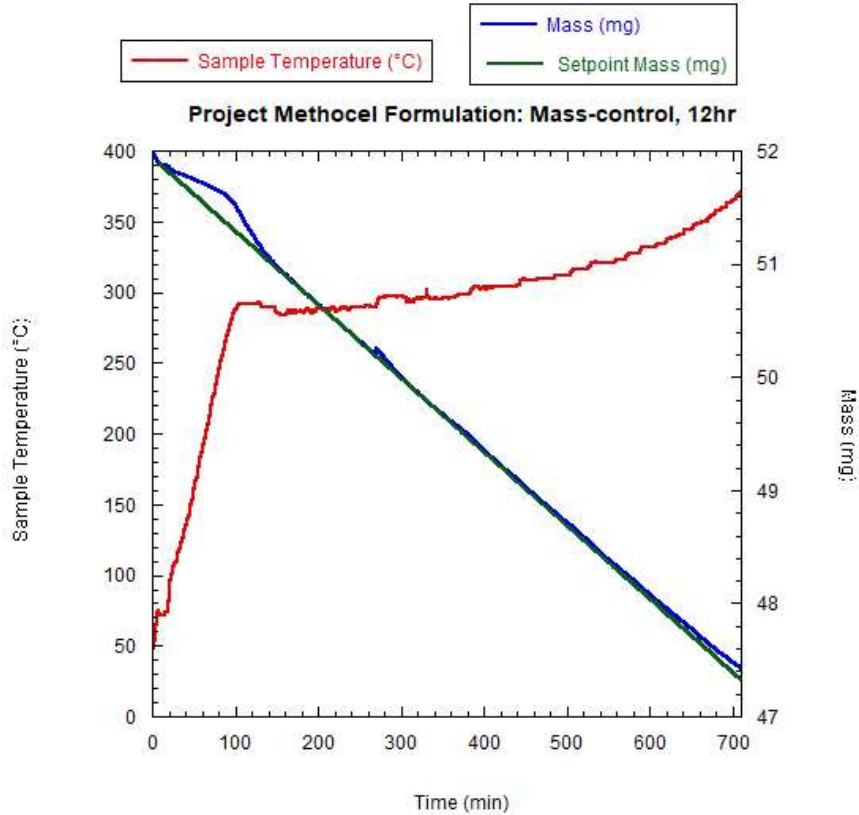


**Figure 7: Mass-loss-rate-controlled thermogravimetric analysis of extrudate fragments in static air, with setpoint a mass loss rate of 0.75 wt.%/hr. This mass curve indicates a mass loss of 8.8 wt.% over 12 h.**

The measured temperature profiles were converted to linear heating rate segments, programmed into the larger furnace for thermolysis steps prior to sintering heat-treatment.

A part produced by Nadler et al. [17] with a complex internal geometry shown in Figure 8 was also characterized. Utilizing Methocel, this extrusion's thermal decomposition was also characterized for comparison to this project. Thermolysis of this sample's shards were investigated with temperature-controlled TG, presented in Figure 99. Most of the organics were lost from 200 to 350 °C.

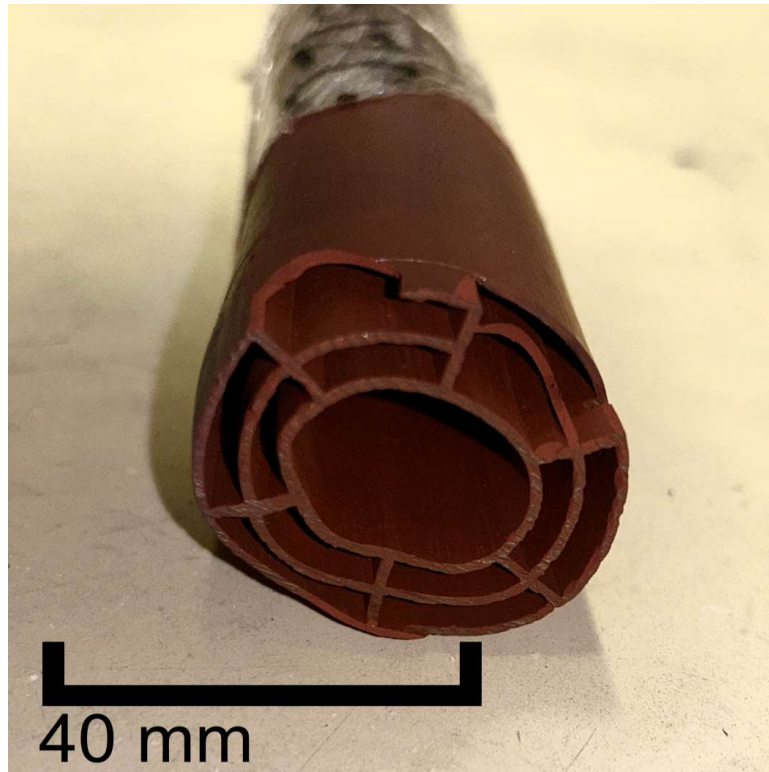


**Figure 8: Linear cellular alloy oxide green body produced by Nadler et al**

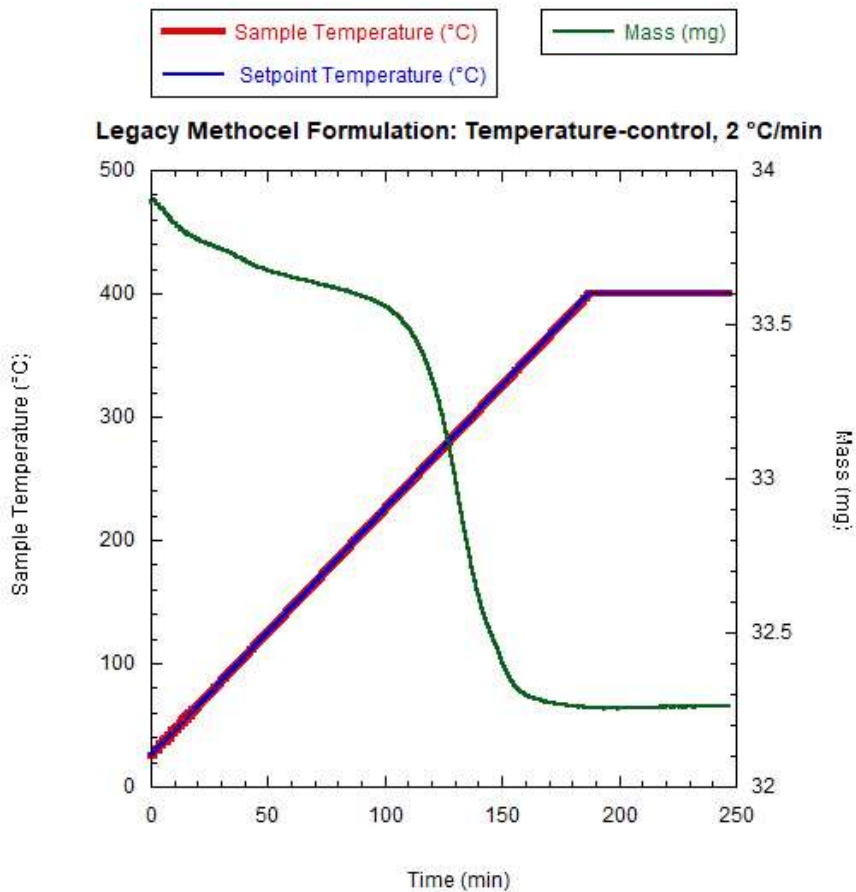


**Figure 9: Temperature-controlled thermogravimetric analysis of legacy project sample fragments in static air, with a heating rate of 2 °C/min and high temperature hold at 400 °C for 60 minutes. This mass curve indicates a mass loss of 4.78 wt.%.**

The temperature zone of significant weight loss was lower for these specimens than the recently extruded specimen investigated in Figure 5. Under rate-controlled TG (Figures 10 and 11), both the 6 and 12 h volatilization remained below 325 °C.

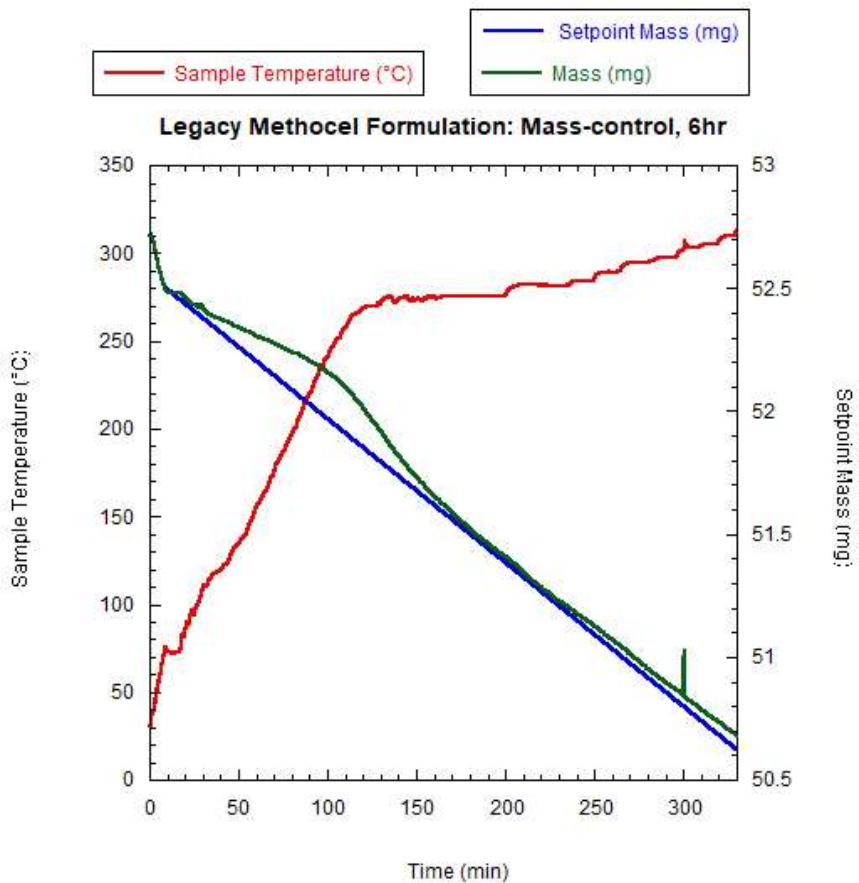


**Figure 10: Mass-loss-rate-controlled thermogravimetric analysis of extrudate fragments in static air, with a setpoint mass loss rate of 0.3 wt.%/hr. This mass curve indicates a mass loss of 3.8 wt.% over 6 h.**

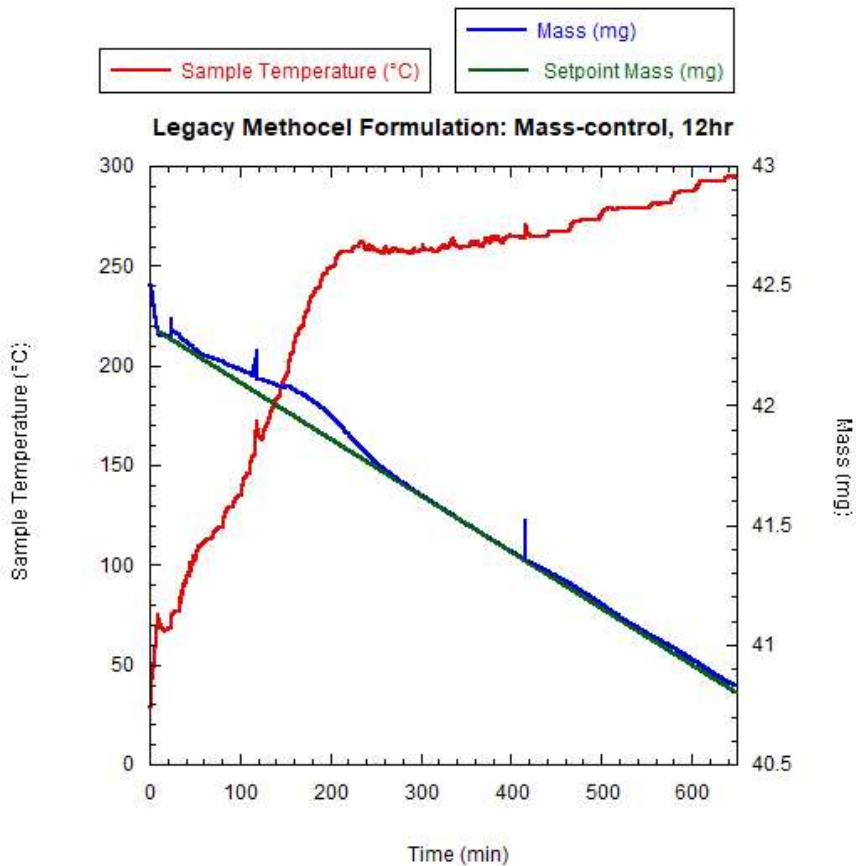


**Figure 11: Mass-loss-rate-controlled thermogravimetric analysis of extrudate fragments in static air, with a setpoint mass loss rate of 0.3 wt.%/hr. This mass curve indicates a mass loss of 3.8 wt.% over 11 h.**

Another binder system designed to be used in fused deposition modeling (FDM) printers was also characterized. PLGA or poly(lactic-co-glycolic) acid, is a block copolymer containing two distinct monomers. Based on temperature-controlled TG plotted in Figure 12, and rate-controlled TG at two different setpoint rates shown in Figures 13 and 14, the volatiles are removed over two distinct temperature ranges.

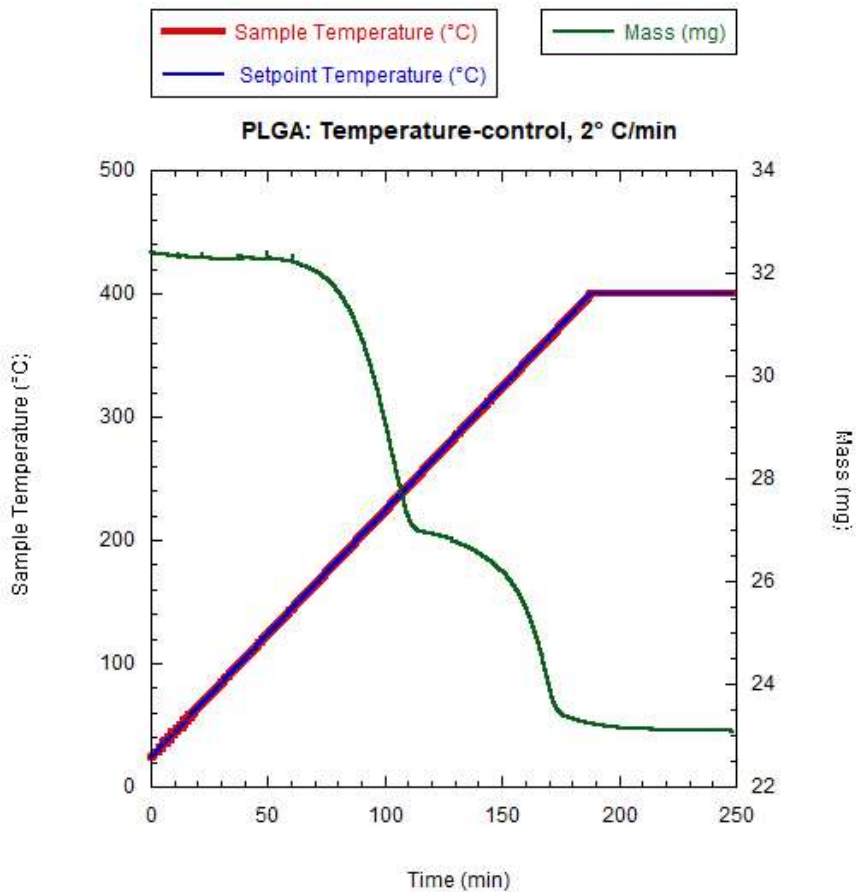


**Figure 12: Temperature-controlled thermogravimetric analysis of printed part fragments in static air, with a heating rate of 2 °C/min and high temperature hold at 400 °C for 60 minutes. This mass curve indicates a mass loss of 28.9 wt.%**

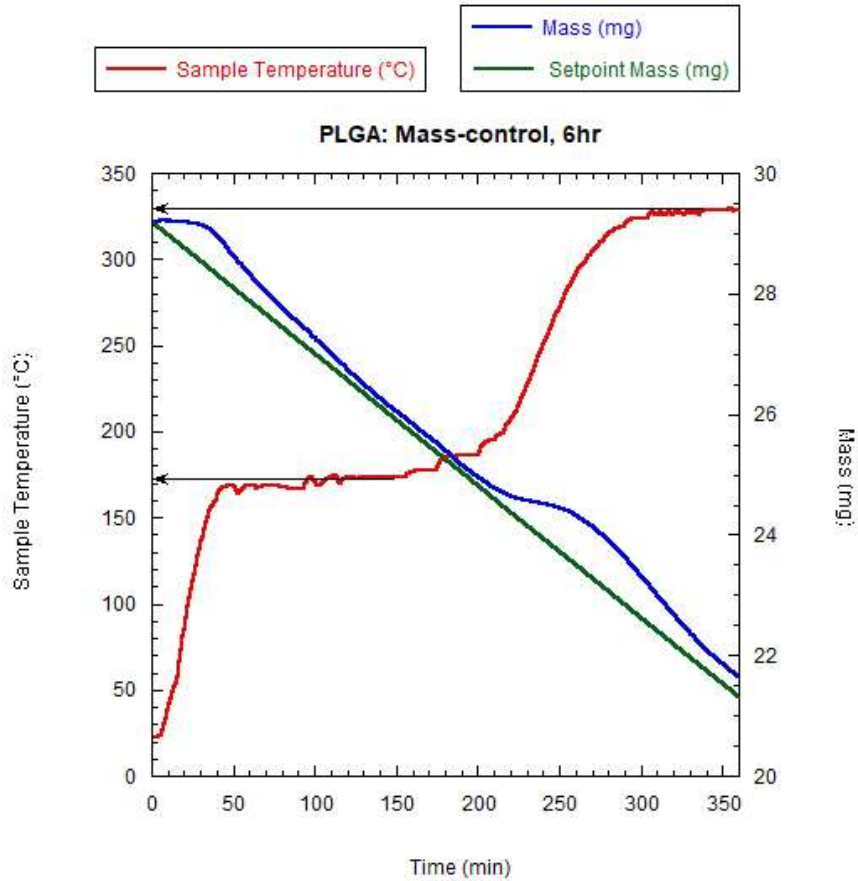


**Figure 13: Mass-loss-rate-controlled thermogravimetric analysis of printed part fragments in static air, with a setpoint mass loss rate of 4.42 wt.%/hr. This mass curve indicates a mass loss of 26.6 wt.% over 6 h. Thermolysis occurs mainly at two temperatures, 172 °C and 330 °C.**

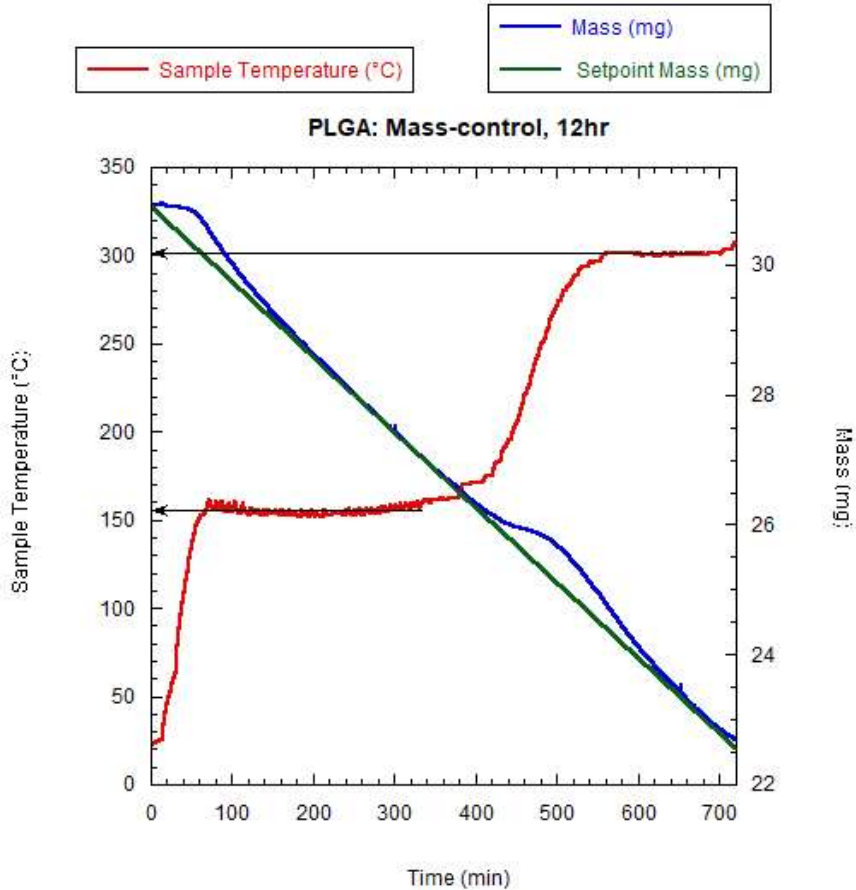


**Figure 14: Mass-loss-rate-controlled thermogravimetric analysis of printed part fragments in static air, with a setpoint mass loss rate of 2.25 wt.%/h. This mass curve indicates a mass loss of 27 wt.% over 12 h. Thermolysis occurs mainly at two temperatures, 156 °C and 300 °C.**

Continuous efforts were made to improve the formulation of the oxide extrudate. Methocel was reduced and a lubricant, Pegosperse-100S, was introduced. Overall organics are lower than in the initial formulation. Due to the similarity in thermal decomposition behavior in Figure 15 to the lower solids formulation, rate controlled thermogravimetry was not performed, and the same initial thermolysis schedule was maintained.

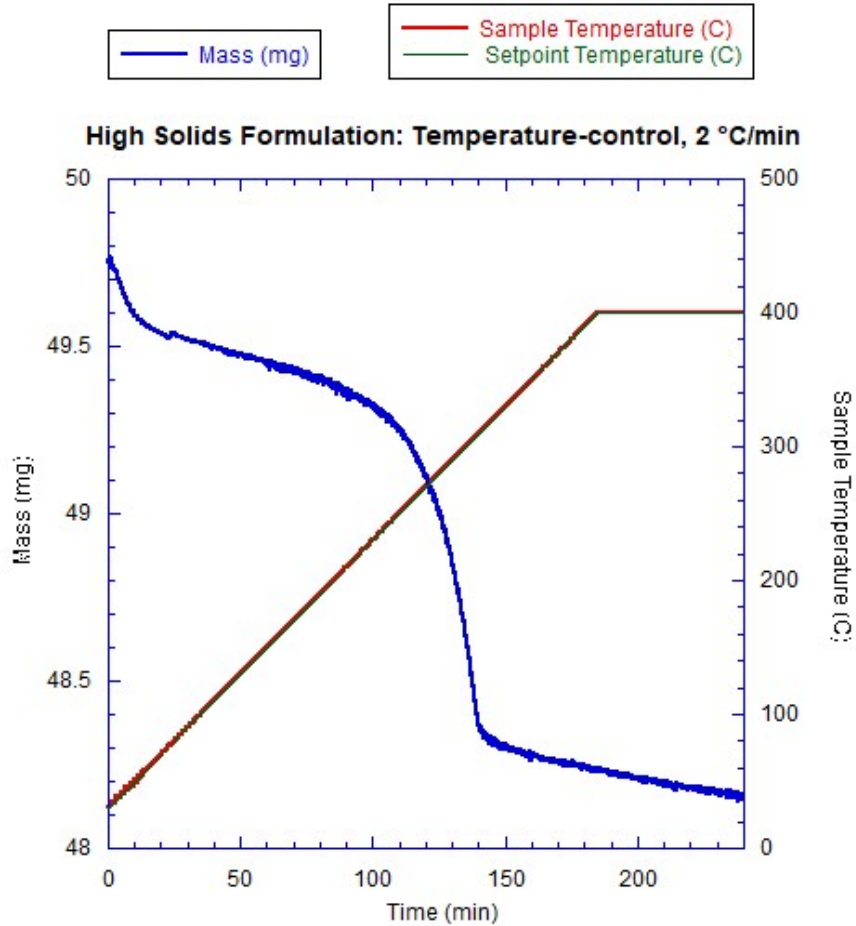


**Figure 15: Temperature-controlled thermogravimetric analysis of high solids formulation sample fragments in static air, with a heating rate of 2 °C/min and high temperature hold at 400 °C for 60 minutes. This mass curve indicates a mass loss of 3.21 wt.%.**

#### 4.1.2 Thermolysis and Sintering Heat Treatments

Specimens were exposed to thermolysis and sintering heat-treatments in the same furnace, the former under flowing air, the latter under He and He/H<sub>2</sub> atmospheres. Some adjustments to the cooling schedules were required after discovering that bubbler fluid was drawn into the furnace chamber from pressures in the furnace dropping below ambient, resulting in a suction action. In following experiments, helium flow was sustained during cooling to a temperature approaching room temperature. Cases in which specimens were

successfully reduced and sintered, an oxide surface scale was observed on the samples, implying either a leak in the seals of the furnace, or back flow of air from the bubbler assembly. Specimens which were not substantially sintered were crushed into powder for x-ray diffraction analysis, while more sintered specimens were ground flat, exposing interior regions to the surface, and that surface was analyzed via x-ray diffraction.

#### *4.1.3 X-Ray Diffraction*

Powder XRD was performed in zero-background silicon sample holders. XRD patterns were compared to patterns in the ICDD database in order to identify phases. All XRD patterns are normalized to the most intense peak in the pattern. In Figure 16, a specimen exposed only to thermolysis heat-treatment consisted predominantly of hematite ( $\text{Fe}_2\text{O}_3$ ) with some peaks corresponding to eskolaite ( $\text{Cr}_2\text{O}_3$ ), and chromite ( $\text{FeCr}_2\text{O}_4$ ). The x-ray diffraction peaks of chromite overlap closely to those of pure  $\text{Cr}_2\text{O}_3$ .

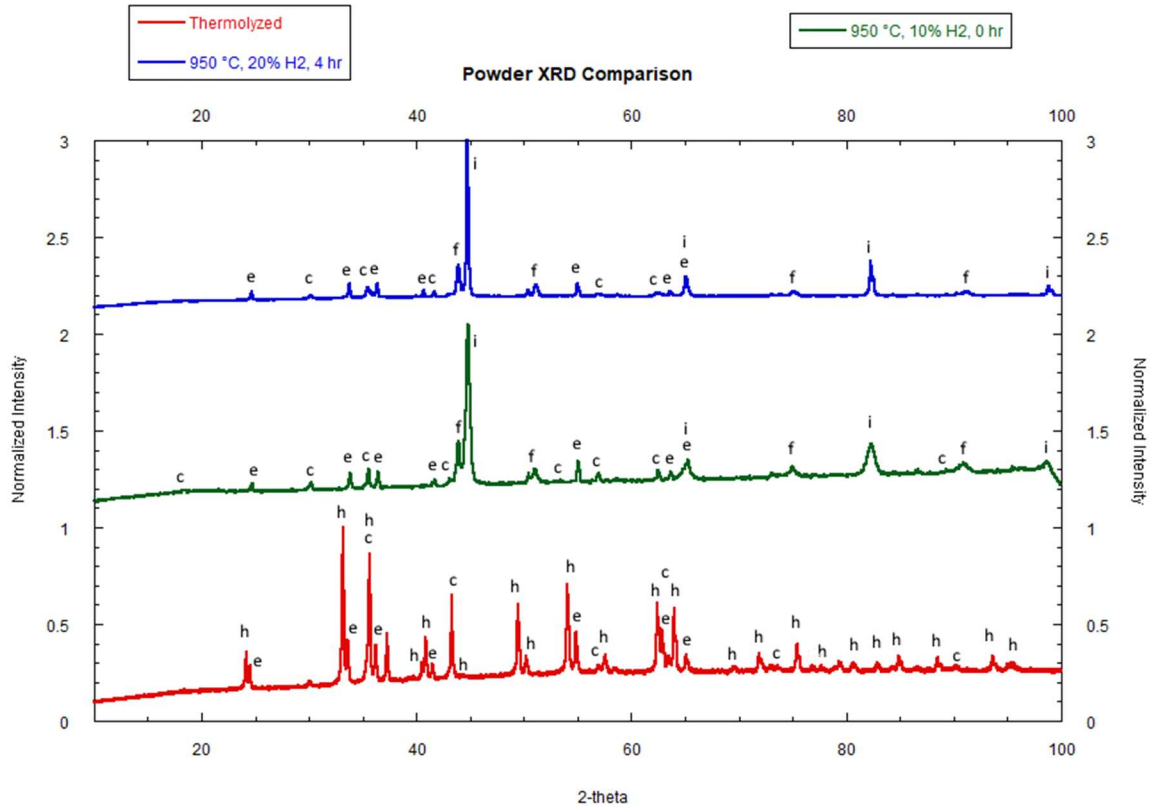


**Figure 16: Powder X-ray diffraction curves for different tested furnace routes. Identified peaks are labeled as h = hematite; e = eskolaite; c = chromite; f =  $\alpha$ -iron; i = synthetic iron; g =  $\gamma$ -iron. Effectively all hematite has been reduced by 950 °C.**

Upon exposure to a reducing atmosphere during a zero or 4 h dwells at 950°C, all hematite was reduced, either to ferrite (BCC) or austenite (FCC), or entered into the chromite spinel. Chromium oxide remains as eskolaite or also enters the chromite phase. In Figure 17, temperature, time, and atmosphere are compared.

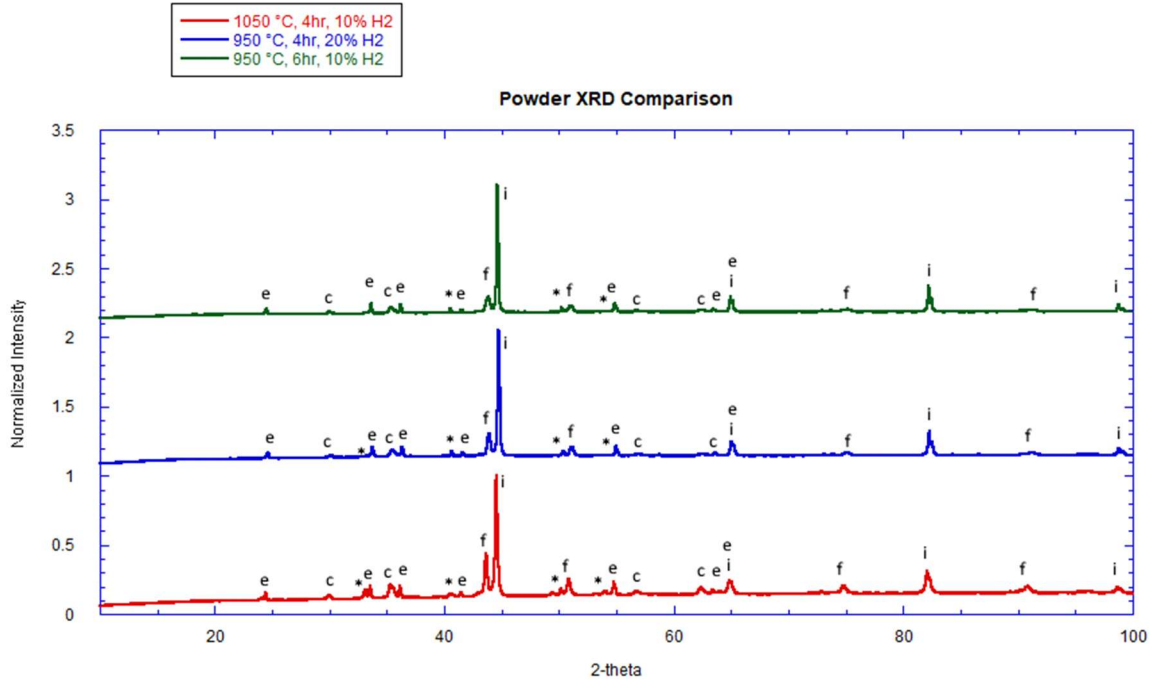


**Figure 17: Powder X-ray diffraction curves for different tested furnace routes. Identified peaks are labeled as h = hematite; e = eskolaite; c = chromite; f =  $\alpha$ -iron; i = synthetic iron \* = unidentified**

No difference in phases present, or relative amounts is apparent for the two different hold times and hydrogen concentrations for the 950 °C dwell temperatures. The dwell temperature of 1050 °C resulted in an increase in the relative intensity of  $\alpha$ -iron peak. There is no apparent diminution in  $\text{Cr}_2\text{O}_3$ -based peaks. However, there is a noticeable shift in the primary synthetic iron peak due to the change in lattice parameter from Cr entering solid solution.

Figure 18 shows diffraction patterns for samples exposed to dwell periods at 1200 and 1250 °C. These diffraction patterns are based on ground and polished sintered specimens, not

crushed into a powder. The 1150 °C sample was still prepared via crushing into a powder and analyzed in a Si holder.

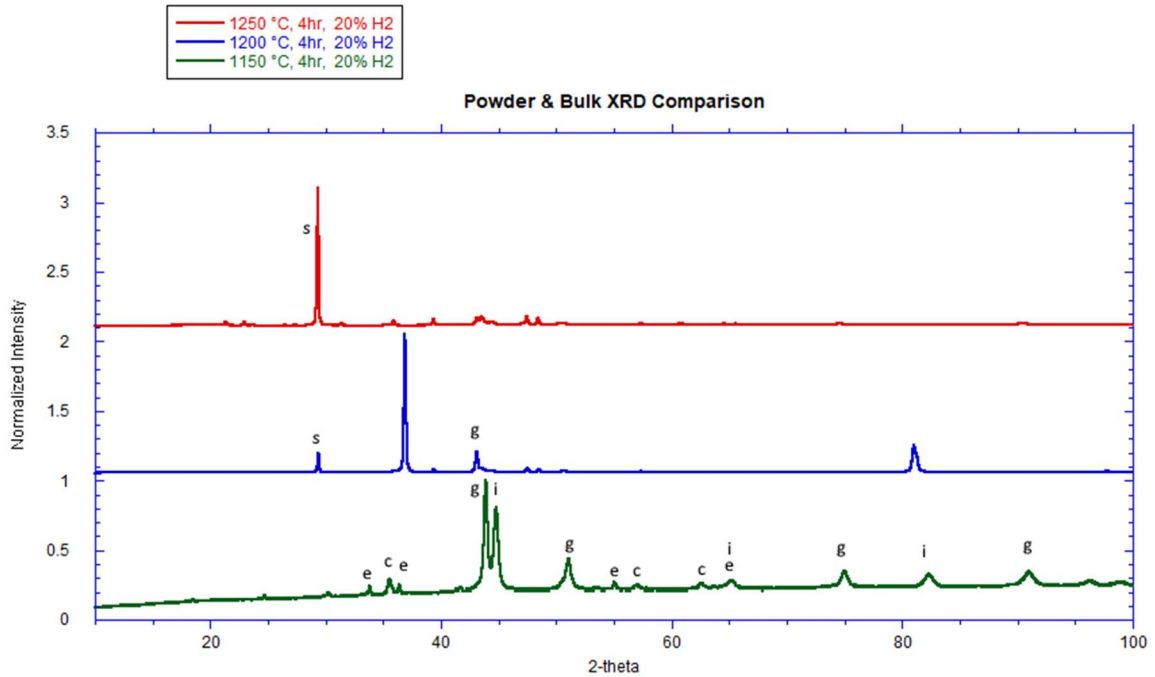


**Figure 18: Powder and Bulk X-ray diffraction curves for different tested furnace routes. Powder bed XRD was performed on the 1150 °C sample, and bulk XRD was chosen for the 1200 and 1250 °C samples. Identified peaks are labeled as h = hematite; e = eskolaite; c = chromite; f =  $\alpha$ -iron; i = synthetic iron; g =  $\gamma$ -iron, s = silicon**

Heat-treatment at 1150 °C shows a significant transformation of  $\alpha$  to  $\gamma$  iron. For the solid specimens, much of the holder material dominated the interaction with the x-ray beam, yielding strong silicon peaks, and minor peaks associated with the sample.

A study of dwell times for a 1200 °C hold is shown in Figure 18. This schedule was applied to the new increased solids loading recipe generated by the Kacher lab, with its thermolysis schedule displayed in Figure 19. While variations in the relative intensities of the oxide peaks are clear, there is no discernable trend with dwell time.

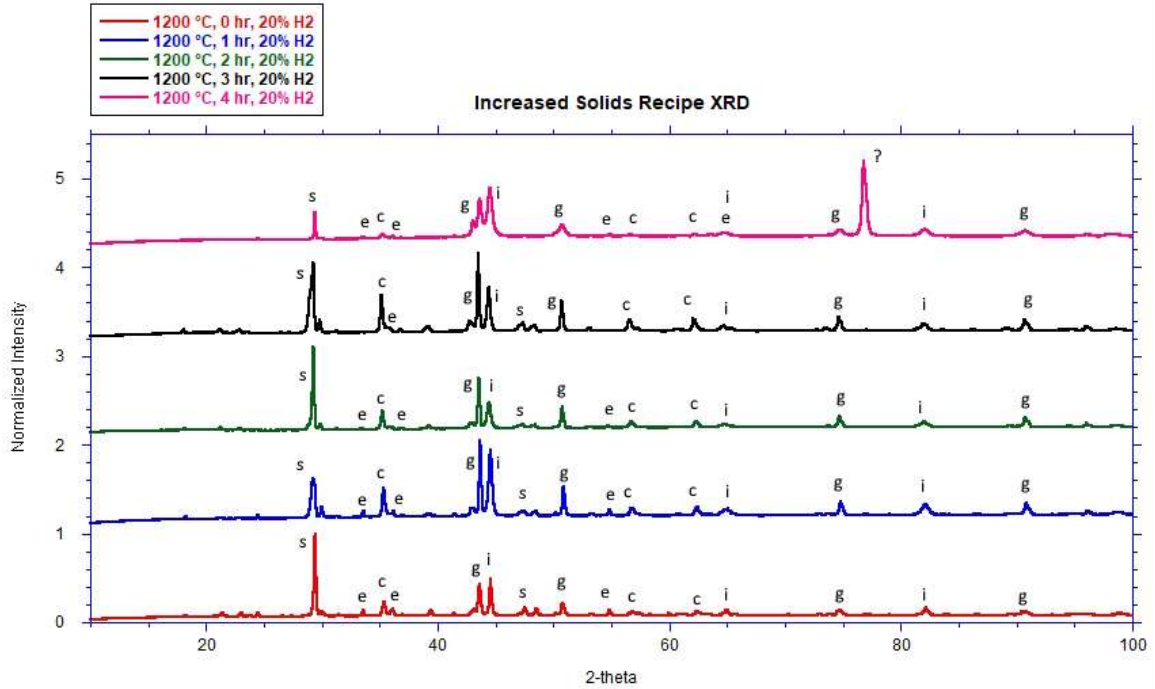


**Figure 19: Bulk X-ray Diffraction curves for tested different furnace routes. Identified peaks are labeled as h = hematite; e = eskolaite; c = chromite; f =  $\alpha$ -iron; i = synthetic iron; g =  $\gamma$ -iron, s = silicon**

These samples also showed silicon peaks associated with the specimen holder. Finally, a 4 h dwell period at 1250 °C was found to be an effective temperature capable of more fully reducing and densifying the higher solids content recipe. A different XRD machine (Rigaku SmartLab SE) more suited for bulk XRD was utilized on the low and high solids loading samples exposed to the same furnace schedule, 1250 °C, 4 hr., at 20% H<sub>2</sub>. The diffraction pattern of the higher solids loading sample is shown in Figure 20. Gamma and synthetic iron identified with relatively diminished peaks associated with chromite.

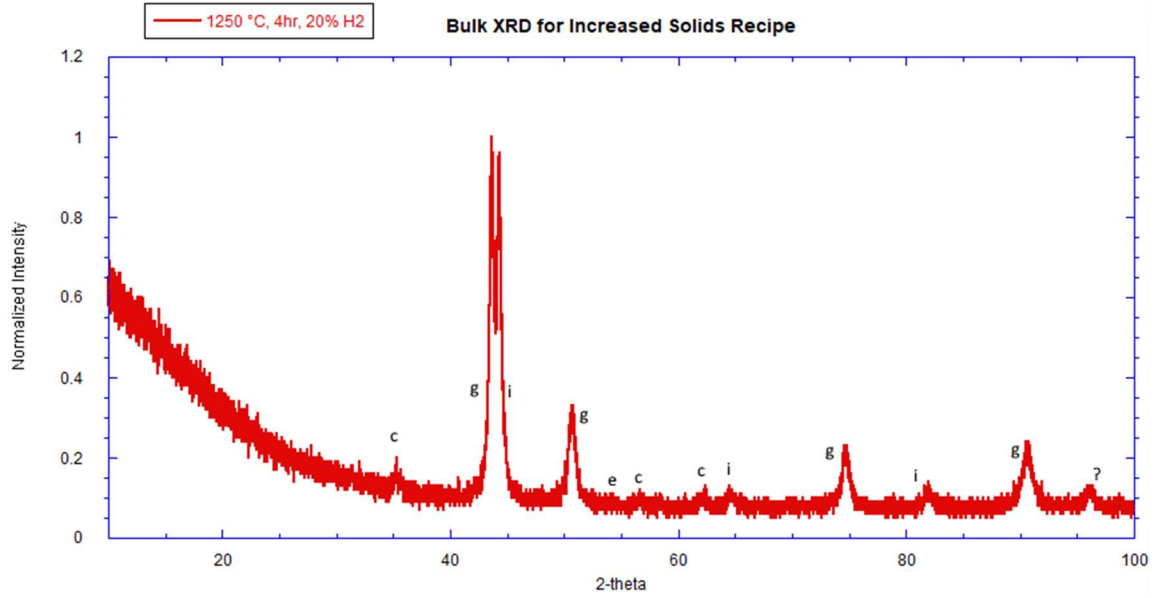


**Figure 20: Bulk X-ray Diffraction curves for tested different furnace routes. Identified peaks are labeled as h = hematite; e = eskolaite; c = chromite; f =  $\alpha$ -iron; i = synthetic iron; g =  $\gamma$ -iron.**

#### 4.1.4 Scanning Electron Microscopy & Energy-Dispersive Spectroscopy

The most metallic sample depicted in Figure 22, 1250 °C 4 hours, 20% H<sub>2</sub>, was polished to a mirror finish and SEM and EDS were performed, with elemental composition displayed in Figure 21. As seen in the EDS scan, iron and chromium are detected in the metal, as well as the presence of Mo, Mn, and Ni.

Map Sum Spectrum		
	Wt%	$\sigma$
Fe	59.5	0.1
Cr	19.0	0.0
Ni	11.4	0.0
O	4.1	0.0
Mo	3.5	0.0
Mn	2.5	0.0

**Figure 21: EDS spectra with calculated weight percent of elements identified for a ground and polished specimen heat-treated at 1250 °C for 4 h.**

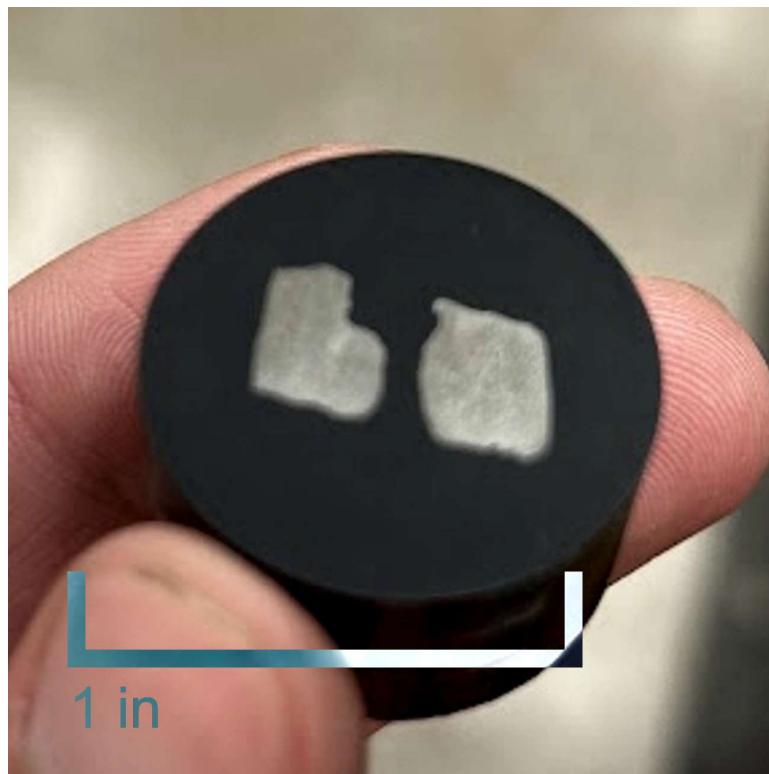


**Figure 22: Reduced low solids sample mounted in conductive epoxy for use in an SEM**

## CHAPTER 5. DISCUSSION

Due to the volume change associated with the thermolysis of the binder, the time scale of several hours was used to de-bind the samples. This helps to ensure that no new defects are introduced through the volatilization or drying of the parts in the first stages of heat-treatment.

Differences in the binder burnouts of the parts produced by Nadler et al. and the current project formulation could be attributed to a few sources. Firstly, there are several grades of Methocel and other related methyl cellulose compounds, like hydroxypropyl methyl cellulose or hydroxyethyl methyl cellulose. These side group changes can alter the rate and temperature at which the species decay through the exchanging of the polymer side groups -H with -CH<sub>3</sub>. Because the legacy samples contained lower amounts of organics (approximately half as much) by weight compared to the low solids formulation, it is also possible that in order to achieve a slower rate of volatilization over the required time the PID control algorithm settled on a lower initial temperature for maximum extraction of organics.

The TG traces of the legacy samples display a 0.67% loss in mass before 100 °C. Being several years old, the legacy sample likely adsorbed atmospheric water as iron oxides and cellulose derivatives like Methocel are hygroscopic. In storage, the sample equilibrated with the atmosphere, drawing most of the moisture to the surfaces of oxide and binder particles.

When removing reduced and densified parts from the furnace, a powdery green surface was sometimes observed. Polishing away the surface of sintered parts with this green cast revealed internal surfaces that displayed a profoundly metallic luster, in spite of its surface layer. High temperature oxidation after the reducing environment is eliminated is likely cause of the observed external oxide layer. Multiple constituents of the alloy composition exhibit a green color upon oxidation, including Ni, Cr, and Mo oxides [9].

When the reducing gas was changed to inert upon cooling, the flow rate was reduced to conserve helium. This reduction in flow rate could cause a pressure drop in the vessel. Connected to a water bubbler for a positive pressure seal, some water vapor might be drawn into the chamber that then acts as an oxidizer. Fluids that could avoid these issues include oils or glycerin.

Another possibility is there is remnant chromium oxide on the surface that is not in enough contact with the catalyzing iron metal during the reduction and sintering process. In combination with a reducing environment that cannot decompose the spinel to reduce it completely, oxides will remain visible and present on the surface, whereas oxides in the bulk are sintered into the metal matrix.

At temperatures exceeding 1000 °C,  $\text{Cr}_2\text{O}_3$  is not present in the equilibrium of metallic alloys exceeding 15 wt.% Cr [10,17]. The stable oxide produced by oxidation of such metal is the spinel  $\text{FeCr}_2\text{O}_4$ . Based on the XRD scan in Figure 16, the primary phase is austenitic gamma (FCC) phase of iron, with several smaller peaks associated with ferrite, the body centered cubic structured, iron phase. The first two metallic peaks share a similar intensity and  $2\theta$  position at approximately 43. It is possible that the minor splitting of x-

ray source from  $\text{Cu-K}\alpha_1$  and  $\text{Cu-K}\alpha_2$ , is causing a doublet to appear for the gamma phase. This is unlikely due to the presence of other BCC iron peaks.

The retained gamma phase, austenite, is due to the addition of alloying elements like nickel and manganese. The BCC structured iron phase corresponds to ferrite and is stabilized by chromium and molybdenum. Based on the structure of alloying elements and EDS scans, it is possible that the ferritic phase is enriched in chromium and manganese, and the austenitic phase is enriched in nickel and molybdenum.

In regard to the other observed peaks, there are some oxide peaks identified in Figure 19. Peaks observed align most strongly with the chromite spinel (311) plane, but the peak could also be attributed to the eskolaite (110) plane [20]. The presence of this mixed oxide in the bulk of the material indicates that this oxide was sealed into the matrix during the sintering process and remained the most stable oxide in the environment at the time of the porosity closing. Chromite formed in this system is due to the reaction between wüstite and eskolaite, at temperatures below 1200 °C [17]. However, dissolved chromium can react to an extent with chromite to yield iron metal and chromium oxide, reducing the ferrous cation present in chromite to iron metal and the chromium cation transforms to pure chromium oxide. At furnace temperatures, the maximum solubility of chromium in iron before chromite reacts to form iron metal and chromium oxide is 1.5 wt.% chromium [17].

## CHAPTER 6. CONCLUSIONS AND FUTURE WORK

The direct hydrogen reduction of metal–metal oxide extrusions mirroring the composition of 316L stainless steel was investigated using X-ray diffraction (XRD) and energy-dispersive spectroscopy (EDS). In addition, the thermal decomposition behavior of several organic additives employed in the extrusion process was characterized via thermogravimetric analysis (TG). Through this combined analytical approach, the minimal temperature, time, and hydrogen gas concentration necessary to achieve effective reduction and sintering of the extrudate were determined. The sequential phase evolution of the material during combined reduction and heat treatment was also identified, providing insight into the reaction pathways and the roles of oxides present in the mixture.

Reduction of the oxide phases occurs progressively throughout the heating process, with sintering and reduction of the particles becoming competing processes at higher temperatures. All initial hematite has been reduced by approximately 950 °C, to either metallic iron or to its +2 oxidation state, present in the chromite spinel. Nickel oxide is similarly reduced to metallic nickel in this temperature range. However, chromium oxide partially reduces and enters the metal solid solution, reacting with wüstite to form chromite, or remaining as unreduced Cr<sub>2</sub>O<sub>3</sub> depending on the local chemical environment and reaction kinetics. This behavior demonstrates importance of local redox equilibria in controlling total composition and microstructural uniformity with hydrogen-based reduction.

The completion of both reduction and sintering was found to depend on the solids loading of the extrudate. Lower solids content formulations achieved reduction and densification at 1200 °C after a four-hour hold, whereas higher solids loading required an increased temperature of 1250 °C for the same duration to reach a similar metallic luster. This relationship emphasizes the coupled influence of diffusion pathways, gas permeability, and particle packing density on reduction kinetics. It further suggests that process optimization for industrial implementation will require precise control of the extrusion composition and green body microstructure to balance strength, porosity, and reduction efficiency.

This work establishes a continued investigation of hydrogen-based reduction of complex-shaped metal–metal oxide extrusions and provides an experimental foundation for extending the technique to other alloy systems and starting materials. Future studies could explore modifications to extrusion feedstock chemistry to target specific alloy groups, including copper alloys & nickel-based superalloys, as well as investigations into alternative reducing atmospheres including ammonia, and the influence of particle size distribution on densification behavior. Microstructural characterization through advanced techniques such as electron backscatter diffraction or transmission electron microscopy could further elucidate the phase transformations and grain growth mechanisms observed here.

Broadly, this research contributes to the field of hydrogen metallurgy, where hydrogen serves as a clean-burning reducing agent capable of reducing carbon emissions in high-temperature metal production. By demonstrating that complex, stainless-steel-like

alloys can be fabricated through a direct hydrogen reduction route, this study provides a meaningful step toward scalable, low-emission metal manufacturing. The insights gained here lay the groundwork for future process optimization, enabling the development of advanced alloys with complex cross sectional geometries while maintaining the technical advantages inherent to hydrogen-based reduction methods.

## REFERENCES

- [1] AIChE Center for Hydrogen Safety, *Hydrogen Flammability, The Elemental Newsletter*, American Institute of Chemical Engineers, New York, NY, USA. [Online]. Available: <https://aiche.informz.net/MailingDesignerSvc/OnlineVersion/preview/mailing/1356218>. [Accessed: Oct. 22, 2025].
- [2] H. A. Alalwan, S. E. Mason, V. H. Grassian, and D. M. Cwiertny, “ $\alpha$ -Fe<sub>2</sub>O<sub>3</sub> nanoparticles as oxygen carriers for chemical looping combustion: An integrated materials characterization approach to understanding oxygen carrier performance, reduction mechanism, and particle size effects,” *Energy Fuels*, vol. 32, no. 7, pp. 7959–7970, Jul. 2018, doi: 10.1021/acs.energyfuels.8b01539.
- [3] M. Al-Buainain and D. C. Dunand, “Sustainable Fe–Cr–Ni stainless steels via hydrogen reduction of blended oxides,” *ACS Sustainable Chem. Eng.*, vol. 13, no. 23, pp. 8687–8698, Jun. 2025, doi: 10.1021/acssuschemeng.5c02264.
- [4] Sigma-Aldrich Inc., *Chromium(III) Oxide Safety Data Sheet*, Version 6.9, Product No. 393703, St. Louis, MO, USA, Oct. 14, 2025. [Online]. Available: Merck KGaA, MilliporeSigma.
- [5] F. Cardarelli, *Materials Handbook: A Concise Desktop Reference*, 3rd ed. Cham, Switzerland: Springer International Publishing, 2018. doi: 10.1007/978-3-319-38925-7
- [6] M. W. Chase, Jr., *NIST-JANAF Thermochemical Tables*, 4th ed. Washington, DC, USA: American Chemical Society; New York, NY, USA: American Institute of Physics for the National Institute of Standards and Technology, 1998.
- [7] H. J. T. Ellingham, “Reducibility of oxides and sulphides in metallurgical processes,” *J. Soc. Chem. Ind. (London)*, vol. 63, no. 5, 1944.
- [8] T. C. Eisele and K. L. Gabby, “Review of reductive leaching of iron by anaerobic bacteria,” *Miner. Process. Extr. Metall. Rev.*, vol. 35, no. 2, pp. 75–105, 2014, doi: 10.1080/08827508.2012.703627.
- [9] Fisher Scientific Company, *Nickel(II) Oxide Safety Data Sheet*, Cat. No. N69-100 / N69-500, Revision 4, Fair Lawn, NJ, USA, Dec. 24, 2021. [Online]. Available: Thermo Fisher Scientific.
- [10] Yu. G. Gurevich, I. D. Radomysel'skii, L. F. Barshchevskaya, N. R. Frage, and Yu. I. Pozhidaev, “Thermodynamic analysis of the reduction of a mixture of iron and chromium oxides by hydrogen,” *Sov. Powder Metall. Met. Ceram.*, vol. 14, no. 1, pp. 13–16, Jan. 1975, doi: 10.1007/BF00804063.

- [11] V. Hynninen, J. Patrakka, and Nonappa, “Methylcellulose–cellulose nanocrystal composites for optomechanically tunable hydrogels and fibers,” *Materials*, vol. 14, no. 18, p. 5137, Sep. 2021, doi: 10.3390/ma14185137.
- [12] C. W. Kovach, *High-Performance Stainless Steels*. Pittsburgh, PA, USA: Nickel Development Institute, Technical Marketing Resources, Inc., 1996.
- [13] O. Kubaschewski and G. Heymer, “The thermodynamics of the chromium–iron system,” *Acta Metall.*, vol. 8, no. 7, pp. 416–423, Jul. 1960, doi: 10.1016/0001-6160(60)90027-4.
- [14] National Institute of Standards and Technology (NIST), *Iron Ore (Labrador) SRM 692 Safety Data Sheet*, Gaithersburg, MD, USA, Jan. 11, 2023. [Online]. Available: <https://www.nist.gov/srm>.
- [15] H. Okamoto, M. E. Schlesinger, and E. M. Mueller, “Cr (chromium) ternary alloy phase diagrams,” in *Alloy Phase Diagrams*, vol. 3, Materials Park, OH, USA: ASM International, 2016, doi: 10.31399/asm.hb.v03.a0006239.
- [16] A. Paaanen and J. Vaari, “High-temperature decomposition of the cellulose molecule: A stochastic molecular dynamics study,” *Cellulose*, vol. 24, no. 7, pp. 2713–2725, Jul. 2017, doi: 10.1007/s10570-017-1325-7.
- [17] J. H. Nadler, *The Hydrogen Reduction of Iron and Chromium Oxides*, Ph.D. dissertation, School of Materials Science and Engineering, Georgia Institute of Technology, Atlanta, GA, USA, May 2003. [Online]. Available: <http://hdl.handle.net/1853/19410>.
- [18] J. Nadler, T. Sanders, J. K. Cochran, and S. S. Kim, “Oxide reduction and diffusion in Fe–Cr alloy honeycombs,” *J. Phys. IV (Proc.)*, vol. 120, pp. 47–54, Dec. 2004, doi: 10.1051/jp4:2004120004.
- [19] D. Spreitzer, *Development of Characterization Methods for the Evaluation of the Kinetic Behavior and the Fluidization of Iron Ore Fines during Hydrogen-Induced Fluidized Bed Reduction*, Doctoral thesis, 2020.
- [20] J. Ralph *et al.*, “Mindat.org: The open access mineralogy database to accelerate data-intensive geoscience research,” *Am. Mineral.*, vol. 110, no. 6, pp. 833–844, 2025, doi: 10.2138/am-2024-9486.
- [21] J. Szekely and J. W. Evans, “Studies in gas–solid reactions: Part I. A structural model for the reaction of porous oxides with a reducing gas,” *Metall. Trans.*, vol. 2, no. 6, pp. 1691–1698, Jun. 1971, doi: 10.1007/BF02913895.

[22] R. Wang, Y. Q. Zhao, A. Babich, D. Senk, and X. Y. Fan, “Hydrogen direct reduction (H-DR) in steel industry—An overview of challenges and opportunities,” *J. Clean. Prod.*, vol. 329, p. 129797, Nov. 2021, doi: 10.1016/j.jclepro.2021.129797.

[23] T. Nishimura, K. Kita, and A. Toriumi, “Evidence for strong Fermi-level pinning due to metal-induced gap states at metal/germanium interface,” *Applied Physics Letters*, vol. 91, no. 12, p. 123123, Sep. 2007. doi: 10.1063/1.2789701.